







The physics of turbulence localised to the tokamak divertor volume

Nicholas Walkden ¹, Fabio Riva ¹, James Harrison ¹, Fulvio Militello¹, Thomas Farley¹, John Omotani¹ & Bruce Lipschultz ²

Fusion power plant designs based on magnetic confinement, such as the tokamak design, offer a promising route to sustainable fusion power but require robust exhaust solutions capable of tolerating intense heat and particle fluxes from the plasma at the core of the device. Turbulent plasma transport in the region where the interface between the plasma and the materials of the device is handled - called the divertor volume - is poorly understood, yet impacts several key factors ultimately affecting device performance. In this article a comprehensive study of the underlying physics of turbulence in the divertor volume is conducted using data collected in the final experimental campaign of the Mega Ampere Spherical Tokamak device, compared to high fidelity nonlinear simulations. The physics of the turbulence is shown to be strongly dependant on the geometry of the divertor volume - a potentially important result as the community looks to advanced divertor designs with complex geometry for future fusion power plants. These results lay the foundations of a first-principles physics basis for turbulent transport in the tokamak divertor, providing a critical step towards a predictive understanding of tokamak divertor plasma solutions.

¹UKAEA, Culham Science Center, Abingdon, Oxfordshire OX14 3DB, UK. ²York Plasma Institute, Department of Physics, Univ. York, Heslington, York YO10 5DD, UK. email: Nick.Walkden@ukaea.uk; James.Harrison@ukaea.uk

Fusion offers the potential of abundant, carbon-free, agile, baseload energy supply to complement renewable generation and meet energy demand in the post-carbon era. The fusion process both requires and generates heat in abundance. A commercially viable fusion plant must be sufficiently available to produce cost-effective energy¹, which in turn requires that any excess heat and particles arising from the fusion plasma must be exhausted without causing performance limiting damage to the device as recognised within mission 2 of the European research roadmap to the realisation of fusion energy². This is a well known challenge given the tolerable heat flux to materials expected from a burning fusion plasma³. Successful deployment of fusion energy is thus contingent on a solution to the challenge of plasma exhaust, which demands a sound understanding of the transport processes within the exhaust volume of the device, called the divertor. The divertor volume most often exists below the X-point of tokamak plasmas (though can also exist at the top of the device in a double null, or upper diverted configuration). The X-point is a null in the poloidal magnetic field that separates the hot core plasma, where magnetic field lines are closed, from walls of the device via a thin external layer of open ended magnetic field lines called the ‘scrape-off layer (SOL)’. The SOL acts as a channel of heat and particles to material surfaces down the divertor ‘legs’. The intensity of plasma transport to material surfaces in the divertor influences the design of tokamak based fusion reactors such as ITER^{4,5}, The EUROfusion DEMO demonstration powerplant design⁶, or the UK STEP (Spherical Tokamak for Energy Production)⁷ design. Indeed in fusion power plants the challenge of successfully exhausting excess heat from the fusion process, and particles including both unspent fuel and helium, is such that conventional divertors may be insufficient and ‘advanced’ divertors are a key area of development for the international community⁸. Advanced divertors generally rely on a modification of the geometry of the divertor legs to realise favourable impacts⁹; an example is the Super-X divertor¹⁰, where the divertor leg is extended to a greater radial location spreading the heat and particles over a larger area and allowing more time for the plasma to cool, which is being tested on the MAST (Mega Ampere Spherical Tokamak) Upgrade device¹¹.

Turbulence within the plasma is commonplace in the edge and SOL regions¹² where severe thermodynamic gradients build up in the plane perpendicular to the magnetic field, and impacts on the performance of the divertor system. Turbulent processes from the hot-core eject plasma into the SOL in discrete structures often called filaments or blobs¹³, which then flow parallel to the magnetic field into the divertor volume. Thermodynamic gradients built up inside the divertor volume in turn provide free energy for localised turbulent transport to redistribute heat and particles deeper into the SOL, or into the private-flux region (PFR)—the region between divertor legs that is un-connected to the upstream plasma. These processes are described schematically in Fig. 1.

Divertor localised turbulent transport has been sparsely studied, yet can have a significant impact on the performance of the device and longevity of divertor components through factors including:

- The onset of divertor detachment¹⁴, a highly radiating state that cools plasma in advance of the material interface → Turbulent cross-field transport within the divertor volume is a key factor determining the heat and particle flux profiles at the divertor target and, therefore, the recycling, ionisation, and recombination rates within the divertor volume which collectively establish the detached plasma state.
- the peak divertor ion and electron temperatures which are a critical parameters determining the sputtering of the

material surface¹⁵ → The peaking of the ion and electron temperature profiles is determined by the respective cross-field transport rate in the divertor volume.

- and, the peak heat-flux to the divertor target which crucially determines the potential for surface melting and damage¹⁶ → The peaking of the parallel heat flux profile is determined by the cross-field transport rate in the divertor volume.

Indeed, the effect of turbulent transport in the divertor must be accounted for heuristically to correctly interpret the profile of the heat flux observed to impinge on divertor surfaces in present day devices (accounted for in the *S* parameter of the commonly used ‘Eich’ fitting function for thermographic measurements of divertor surface heat fluxes)¹⁷. This broadening produced by divertor transport can have complex behaviour, for example differing between inner and outer divertor legs on MAST¹⁸ or weakly depending on divertor leg length on the TCV (Tokamak à configuration variable) device¹⁹. Despite the impactful and complex role played by divertor transport, there is no established first-principles understanding of cross-field transport in the divertor volume. Laminar simulations, often the tool of choice to interpret edge and divertor physics in present day experiments, and to design future ones, employ ad-hoc transport coefficients to capture this effect which do not account for any dependence of turbulent transport on the geometry of the divertor configuration. The scale of the transport that must be set in laminar simulations to match experiments is anomalously high, and cannot be accounted for by collisional transport processes. As such, setting a physics basis for turbulence in the divertor volume is important both for present day interpretation and predictive design of future devices, particularly those with advanced divertors. Despite a relative sparsity of literature concerning the physics of divertor localised turbulence, there exists a significant and growing empirical basis. High speed imaging is a commonplace technique used to analyse turbulence in the tokamak boundary, and has revealed turbulent structures in the divertor volume of tokamak devices including NSTX (National Spherical Torus Experiment)^{20,21}, Alcator C-Mod^{22,23}, TCV²⁴ and MAST^{25–28}. Concurrently, advanced tomographic inversion methods for 3D structures in high speed imaging data^{29,30} have been developed to allow deeper analysis of this complex imaging data, whilst the fidelity of non-linear simulations of turbulent phenomena is growing. The STORM (Scrape-off layer Turbulence ORiented Module) module^{31,32} of the BOUT++ (BOUndary Turbulence++) framework^{33,34}, for example, produces high fidelity simulations of tokamak boundary turbulence and has recently been validated against experimental measurements of the motion of individual turbulent structures³⁵ and separately against full scale turbulence³⁶ in the upstream region (immediately adjacent to the core plasma) of the MAST device.

This article presents results, developed through a combination of experimental measurement utilising advanced tomographic inversion and state-of-the-art simulation using STORM that advance the knowledge base of key turbulent transport processes that occur in the divertor. These results lead to the statement of a simple hypothesis regarding the impact of the geometry of the divertor system on turbulent transport flowing into the PFR, potentially relevant to fusion power plant designs as they increase focus on ‘advanced’ divertors with modified geometry⁸, and the MAST Upgrade device¹¹ engages in future experimental campaigns to investigate such designs. The results of this work provide the foundations of a first-principles physics basis ultimately needed for full predictability of the overall divertor plasma solution and performance, and demonstrates a leading order impact of the divertor geometry on turbulent transport levels.

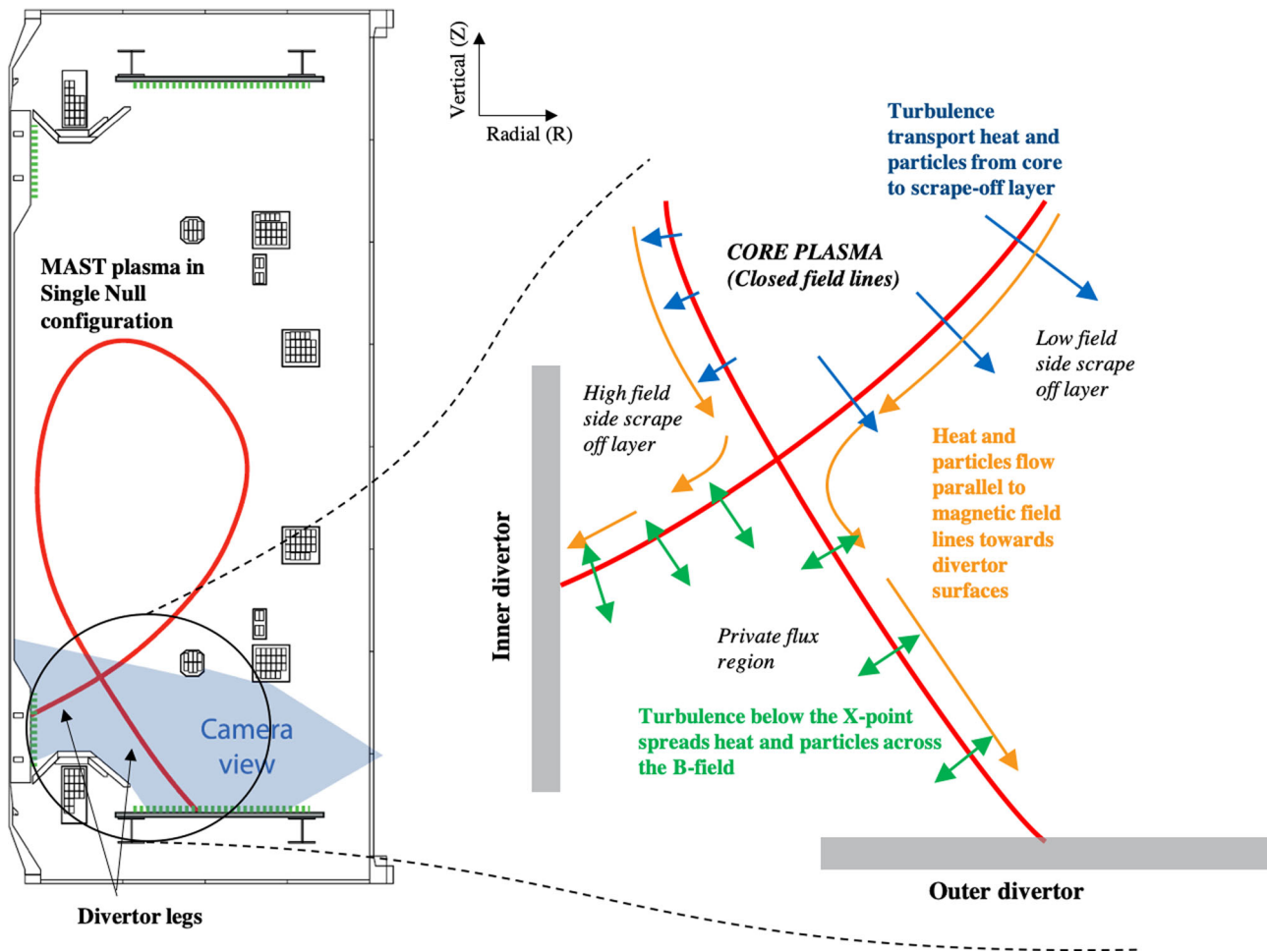


Fig. 1 Schematic illustration of turbulent and parallel transport processes in the divertor volume. Turbulence in the hot core ejects particles and heat into the scrape-off later (SOL) (blue arrows) which flows along magnetic field lines into the divertor volume (orange arrows), to be re-distributed into the SOL and private-flux region (PFR) (green arrows) in divertor legs before intersection with material surfaces.

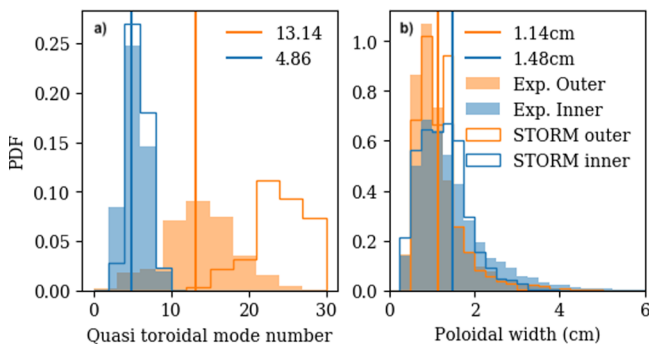


Fig. 2 Spatial distribution and width of turbulent structures in the divertor. **a** Quasi-toroidal mode number and **(b)** poloidal Full-Width Half-Maximum cumulative distributions of turbulent structures across all discharges detailed in table 1. Mean values are represented by vertical lines. Data from the simulation³⁶ is shown as solid lines, whilst experimental data as filled histograms. The clear separation in the histograms of toroidal mode number between inner and outer legs demonstrate strong evidence that turbulence in the two legs is independent.

Results

Shape, distribution, and spectra of turbulent structures in the divertor. Figure 2 shows cumulative measurements of the mode

number (panel 2a) and width (panel 2b) of turbulent structures in both inner and outer divertor legs of the MAST device across the experimental database utilised in this article as a histogram. Figure 2a demonstrates a clear separation in the histograms of the quasi toroidal mode number between inner and outer divertor legs. If turbulent structures in one leg were connected (along the path of magnetic field lines) to the other, then this mode number would necessarily be equal in both. The clear separation of the histograms therefore demonstrates that turbulent structures in the inner and outer divertor legs are isolated from one another. This corroborates measurements made on specific discharges in the NSTX device (a sister spherical tokamak to MAST)²¹, agrees with the predictions of linear analysis based on the resistive ballooning and flute instabilities³⁷, and suggests that this feature is ubiquitous to divertor turbulence (at least in spherical tokamaks).

The STORM simulation reflects the qualitative trend found in experiment, with a significant difference in mode numbers measured in the inner and outer legs and a well reproduced toroidal mode number distribution in the inner divertor leg. The simulation exhibits a tendency towards higher mode numbers in the outer divertor leg than the experiment, possibly indicating higher wavenumber turbulence generated in the simulation than in reality. Also shown in Fig. 2, the poloidal filament widths in both inner and outer legs are similar and the simulation faithfully reproduces the scale of turbulent structures derived from

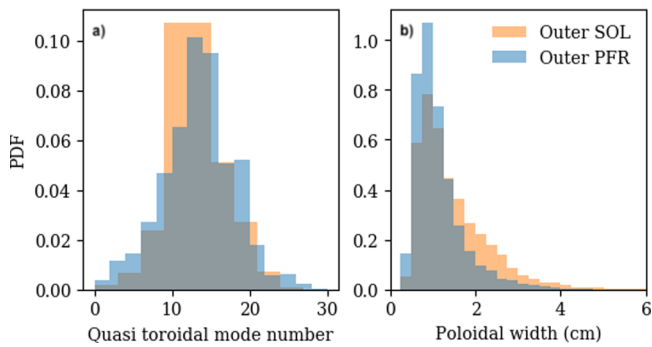


Fig. 3 Spatial distribution and width of turbulent structures in the outer divertor leg. **a** Quasi-toroidal mode number and **(b)** poloidal Full-Width Half-Maximum (FWHM) cumulative distributions of turbulent structures across all discharges detailed in table 1 for the private flux region (PFR) at $\psi_N = 0.99$ (blue) and scrape-off layer (SOL) at $\psi_N = 1.01$ (orange) of the outer divertor leg where ψ_N is the normalised poloidal flux coordinate.

experimental measurements. Despite both divertor legs showing similar real-space widths, the variation in magnetic field strength from inner to outer leg means that, relative to the Larmor radius, $\rho_s = \sqrt{T_e m_i / eB}$ (≈ 0.5 mm for the inner and ≈ 1 mm for the outer), the inner-leg structures are 2–3 times larger than the outer leg. In both of the quantities analysed the individual histograms from each discharge (omitted from Fig. 2 for clarity) match closely the cumulative histograms shown in Fig. 2, indicating that the observations made are insensitive to the parameters of the plasma within the ranges considered (which largely cover the operational range available) and are thus reasonably considered fundamental to the properties of the turbulence observed in the MAST divertor. This is true even for a comparison between L-mode and H-mode, though note that the H-mode studied here is the exotic ELM-free state, used so that sufficient statistics could be generated without ELM events contaminating the measurement. The H-mode measurements demonstrate consistent separation of toroidal mode numbers in inner and outer divertor legs, and similar poloidal filament widths to L-mode measurements. Filament widths in the outer divertor leg are slightly larger in the H-mode measurement, however this may be an impact of statistical error given the relatively small sample size in each shot individually.

The measurements presented in Fig. 2 focus on the PFR in the inner and outer divertor legs. In principle the SOL of the outer divertor leg is also accessible within the plane used for poloidal inversion. Figure 3 shows the cumulative histograms of quasi-toroidal mode number (3a) and poloidal filament width (3b) in the SOL of the outer leg at $\psi_N = 1.01$, and compares these to the histogram of the outer leg at $\psi_N = 0.99$. The measurements are similar in almost all respects, with the exception of a tail of larger structure widths measured in the SOL. Within the SOL structures from upstream are also present in the divertor, though typically outside $\psi_N = 1.01$ ^{27,28}. However, these structures are observable within the inversion data analysed in this paper, and it is plausible that these upstream filaments may interfere with measurements made in the SOL. For this reason, the difference observed in poloidal widths in Fig. 4 may be attributed to interference by the larger upstream filaments.

The spectral characteristics of the turbulence were also investigated on the same PFR flux surfaces as in Fig. 2 from the tomographically inverted experimental and simulation data, and demonstrate poloidal wavenumbers in the range $|k_\theta| \rho_s < 0.4$ for the outer divertor leg and $|k_\theta| \rho_s < 0.2$ for the inner across a broad frequency band up to and above 40 kHz, as shown in Fig. 4. Measurements in simulation and experiment are

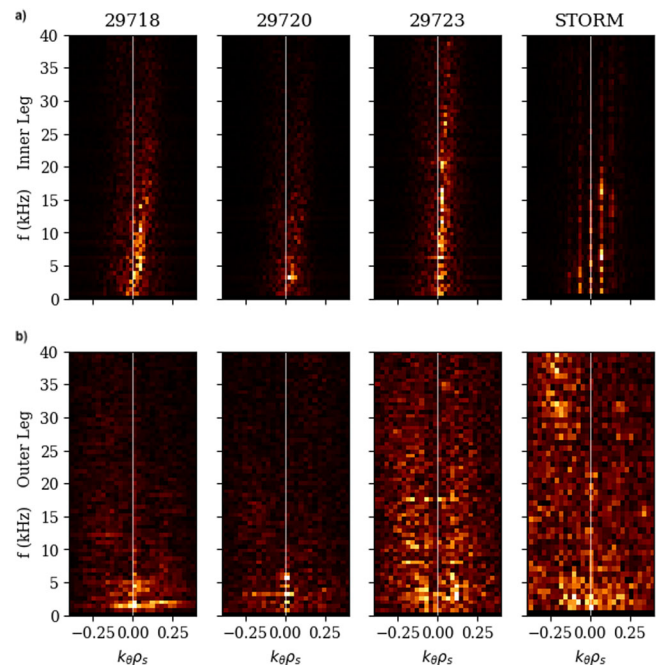


Fig. 4 Turbulent spectra in inner and outer divertor legs. Wavenumber (relative to larmor radius) and frequency spectra from the $\psi_N = 0.99$ surface from the inner (row **a**) and outer (row **b**) divertor legs where ψ_N is the normalised poloidal flux coordinate. Three experimental examples are provided from the database outlined in table 1 alongside the simulation in the four columns as labelled. All data are shown on a consistent, arbitrary linear scale.

consistent (noting a more modal behaviour in the simulation which is due to a toroidally periodic domain with a period of π radians). The condition of $k_\theta \rho_s < 1$ is well satisfied in both divertor legs, which is a key condition for the application of drift-reduced fluid models³⁸ such as that used in the STORM model that the simulations considered here are based on. This indicates that the class of model used in simulations here can be considered reasonable for turbulence localised to the divertor volume.

Turbulent flow in the inner divertor leg. Figure 5 a shows an example of a 2D map of the turbulent flow of an individual discharge from the experimental database, calculated in the inner divertor. The features in this example are typical to all shots analysed, and show structures moving dominantly poloidally (along the projection of magnetic field lines, the θ direction) near to the separatrix but dominantly radially (the ψ_N direction) deeper into the PFR. To compare the flows across the database, the vectors are decomposed into directions parallel (Fig. 5b) to and perpendicular (Fig. 5c) to the projected magnetic field lines and averaged. The discharges with plasma current of $I_p = 400$ kA, which matches the conditions used for the STORM simulation, are highlighted in blue.

There is a net flow of turbulent structures in both the radial and poloidal directions that exhibits broadly similar behaviour across the database. Near to the separatrix, the flow measured in the inner leg is directed poloidally towards the divertor target but transitions to a radial flow in the far PFR. The profiles and magnitudes of the flow measured in the simulation match that of the experimental dataset well in the vicinity of the separatrix but the radial flow is suppressed in the far PFR suggesting that the transport level in the simulation may be an under-estimation of experiment. In the deep PFR turbulent structures in the

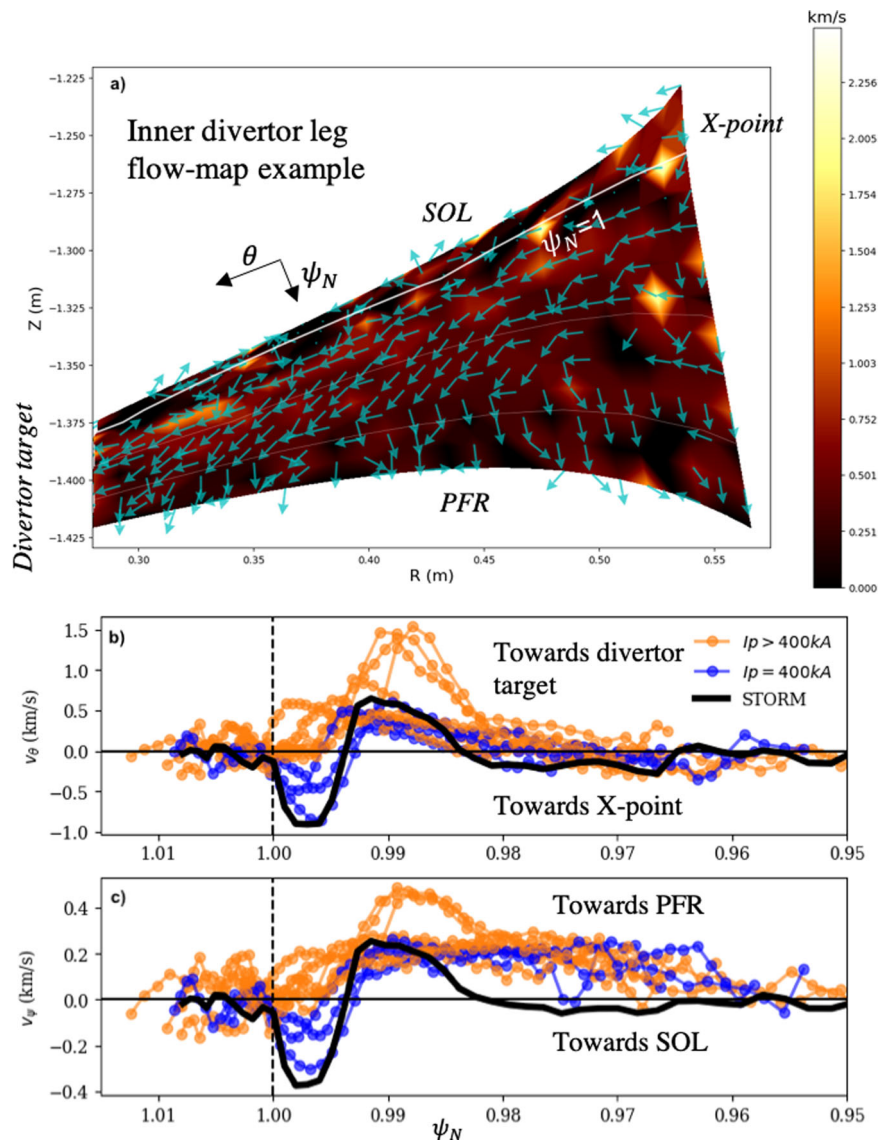


Fig. 5 Turbulent flow measurements in the inner divertor leg. **a** Example of a flow map measured in the inner divertor leg for a typical discharge showing scrape-off layer (SOL) and private-flux region (PFR) flows with the separatrix ($\psi_N = 1$ magnetic flux surface where ψ_N is the normalised poloidal flux coordinate) shown as a white line. **b** Poloidal (θ direction) and **c** radial (ψ_N direction) flows in the inner divertor leg averaged poloidally for all plasmas in the database. Blue traces indicate plasmas with a plasma current $I_p = 400$ kA (matching conditions used for the STORM simulation) whilst orange traces indicate plasmas with $I_p > 400$ kA.

simulation are observed to decay within the inter-frame time of the synthetic movie and are therefore not trackable by the velocimetry which is based on frame-to-frame correlations, indicating that losses in the simulation (dominantly parallel losses) may be exaggerated compared to experiment. The poloidal flow is directed towards the target in the PFR and away from the target in the SOL of the inner divertor leg. Taking $v_\theta \sim 0.5$ km/s from Fig. 5, and reasonable estimates of $n_e \sim 0.6 \times 10^{19} \text{m}^{-3}$ and $T_e = T_i = 20$ eV for the electron density and electron/ion temperature respectively, gives a convected heat flux of 0.05 MW/m^2 towards the target. This is around 25% of the typical heat flux measured at the MAST inner target (0.2 MW/m^2 as measured by ref. ¹⁸) indicating that the contribution of poloidal cross-field flows to target heat fluxes in MAST may be significant. Interrogation of the simulations reveals that the poloidal flow of turbulent structures is likely an entrainment in the $\mathbf{E} \times \mathbf{B}$ flow due to the sheath potential, whilst the radial flow is due to the cross-field propulsion of turbulent structures.

Turbulence drives in inner and outer divertor legs. Reasonable agreement between the nonlinear fully turbulent STORM simulation and measurements across the MAST experimental database has been demonstrated both qualitatively and quantitatively within this article. There are over estimates in the STORM toroidal mode number in the outer divertor leg, and underestimates in the turbulent radial flow into the far PFR of the inner leg, however the leading order details of the turbulence are well reproduced. On this basis, the simulation has been used to diagnose the origin and drive of the turbulence by calculating the turbulent cross-field heat flux in both divertor legs, comparing simulations with various turbulent drive terms negated in succession.

Figure 6 compares the poloidally averaged turbulent cross-field heat flux for each simulation case with different drive terms eliminated with the full simulation in each divertor leg. In interpreting Fig. 6, the reader should compare each coloured line in turn to the black line to infer the effect of each of the classes of

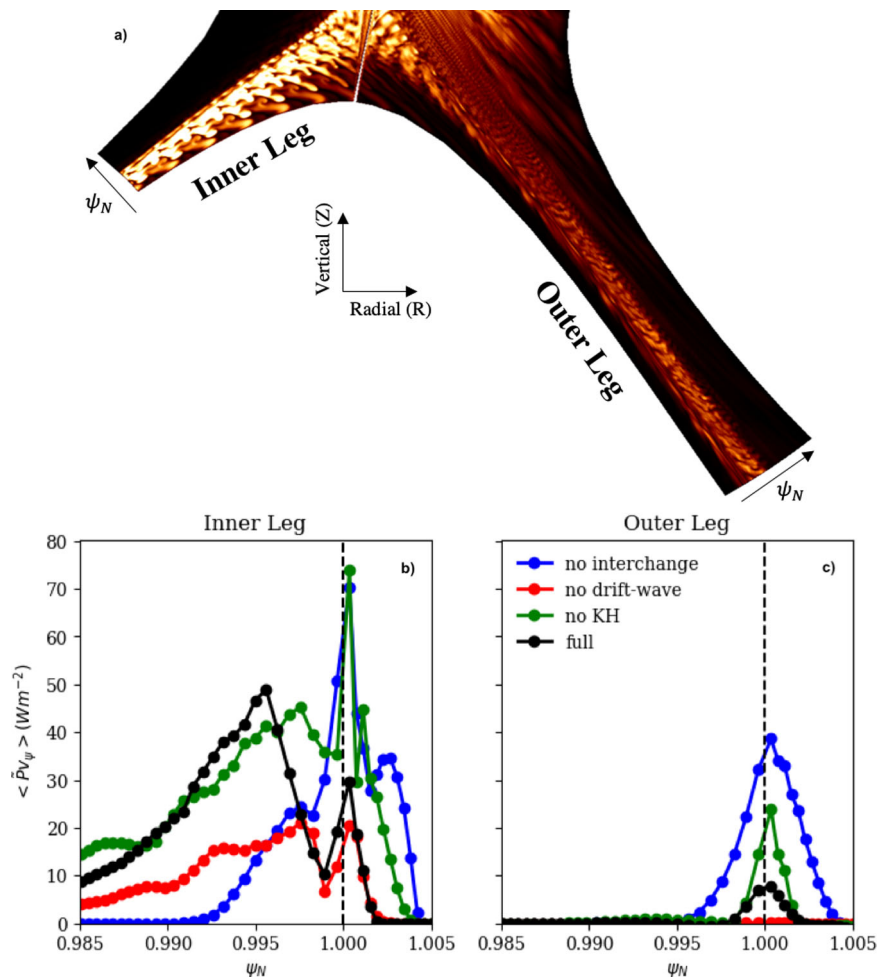


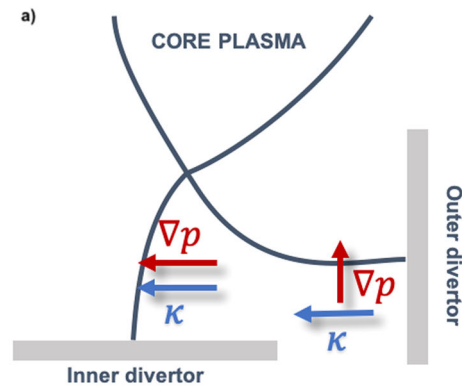
Fig. 6 Heat flux from simulated divertor turbulence. **a** Example of the poloidal structure of the plasma density in the divertor of the STORM simulation analysed. Poloidally averaged turbulent radial heat fluxes into the PFR in STORM simulations of MAST³⁶ in the inner (**b**) and outer (**c**) divertor legs. Fluxes are compared between the full simulation (black) and simulations with interchange (blue), drift-wave (red) and Kelvin-Helmholtz (green) turbulence removed respectively. A positive flux indicates transport into the private flux region (PFR). ψ_N is the normalised poloidal flux coordinate, \bar{P} is the electron pressure fluctuation and v_{ψ} is the turbulent convective velocity in the ψ_N direction.

turbulence. Turbulence in the inner divertor leg spreads heat more effectively into the PFR than in the outer, consistent with thermographic measurements made by ref. ¹⁸. This is demonstrated qualitatively in the cross-section from the simulation, shown in Fig. 6a, where significantly more turbulence activity can be seen in the inner divertor leg than the outer, and quantitatively by comparing the peak heat flux calculated in each divertor leg in Fig. 6b, c. The nature of the turbulence in the PFR of the inner-leg can be classed drift-interchange, with a clear reduction in the heat-flux occurring when either resistive drift-waves or interchange turbulence is removed from the system. Kelvin-Helmholtz (KH) turbulence is not a driver, but close to the separatrix shear-flow effects are stabilising as their removal leads to higher transport fluxes. The inner-leg PFR is a ‘bad-curvature’ region, where thermodynamic gradients are parallel to the curvature vector of the magnetic field, and is analogous to the low-field side SOL. In bad-curvature regions magnetic curvature drives turbulence, as demonstrated by Fig. 6. By contrast, the outer-leg PFR is a ‘good-curvature’ region and the removal of interchange effects leads to an increase in the radial heat flux (directed into the PFR). Once again in the outer divertor leg KH instabilities are not present and shear flows are stabilising near the separatrix. The turbulence in the outer leg arises from unstable drift-waves, the removal of which completely suppresses

radial heat transport into the PFR and the turbulence may be classed as drift-wave turbulence. For like-for-like conditions, the difference in turbulence between inner and outer legs implies that the inner leg will exhibit enhanced transport into the PFR compared to the outer—an effect that is rarely if ever represented in ad-hoc transport used in laminar modelling of the divertor. It is notable that this effect relies only on the geometry of the divertor legs, so is likely to be ever-present other than for deeply exotic configurations. The important and contrasting role of the magnetic curvature demonstrates that it is a leading order actuator to vary turbulence levels in divertor legs. This statement allows for the postulation of a simple hypothesis: The orientation of a divertor leg in the poloidal plane has a leading order impact on the level of localised transport due to divertor turbulence. The destabilising/stabilising effect of the magnetic curvature is maximised when a divertor leg is vertical, since thermodynamic cross-field gradients are fully parallel/anti-parallel to the curvature vector. Conversely the effect of magnetic curvature is minimised in a horizontal divertor leg as gradients are perpendicular to the curvature vector. In principle the effects described would be opposite in the SOL where gradients are respectively reversed, however light levels in the inner leg SOL prevent any measurement of turbulence there and the outer leg SOL is dominated by turbulence originating above the X-point,

Curvature driven transport is maximised when the pressure gradient ∇p is parallel to the curvature vector κ

Maximised transport configuration



Minimised transport configuration

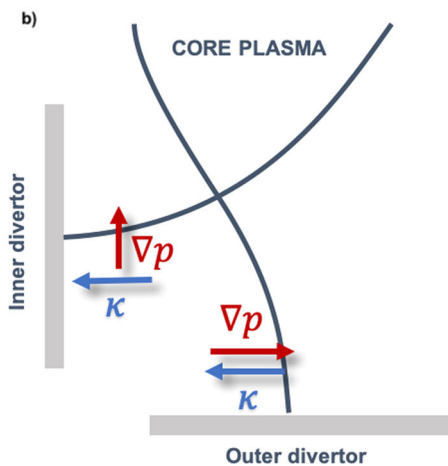


Fig. 7 Schematic illustration of the impact of divertor geometry on turbulence levels. Configurations showing proposed divertor geometry configurations that maximise (a) and minimise (b) turbulent transport from the scrape-off layer (SOL) into the private flux region (PFR) due to the alignment/misalignment of the pressure gradient in the PFR and the magnetic curvature vector. ∇P is the gradient of the electron pressure and κ is the magnetic curvature vector.

so there is not sufficient basis to make statements about these regions. Drift-wave turbulence is ever-present, however the impact of magnetic curvature can enhance/suppress the turbulence level. This means that transport into the PFR is maximised in the inner divertor leg when it is angled normal to the radial direction because the destabilising effect of magnetic curvature enhances transport. Transport into the PFR is maximised in the outer divertor leg when it is angled horizontally (parallel to the radial direction) because the stabilising effect of the magnetic curvature is minimised. This hypothesis is illustrated schematically in Fig. 7.

The impact of divertor leg geometry on divertor leg transport is potentially important for the understanding of future power-plant divertor designs, where advanced concepts such as the ‘Super-X’ divertor^{10,39,40} are being considered. The Super-X divertor, which is characterised by a long, near radial divertor leg, is being prototyped on MAST Upgrade¹¹ with exceptional diagnostic coverage. The results presented in this paper imply

that such a configuration should maximise the rate of turbulent transport from the SOL into the PFR in the outer divertor leg; a potentially testable hypothesis. Moreover, all of the effects discussed are likely to present strongest in tight aspect ratio devices due to their reduced major radius and, therefore, increased magnetic curvature.

Conclusions

This article combines advanced measurement techniques of high speed camera footage, a novel tomographic reconstruction method, and high fidelity turbulence simulations to assess the physics of localised turbulence in the divertor volume of the MAST device. The simulations reproduce the spectral characteristics, size, distribution, and flow of turbulent structures within the divertor volume. These characteristics are found to be largely invariant across a wide experimental dataset indicating that divertor turbulence is insensitive to operational parameters and ubiquitous in MAST. Turbulence in the two divertor legs is decoupled and radial heat transport from the SOL into the private flux region in the inner divertor is stronger than in the outer due to the effects of magnetic curvature. The simulations demonstrate that unstable resistive drift-waves contribute to turbulence in both divertor legs. Magnetic curvature further destabilises the inner divertor leg and the turbulence is therefore classified as drift-interchange, whilst it has a stabilising effect in the outer leg where the turbulence is classified as drift-wave. This indicates that modification of divertor leg geometry may offer a route towards optimising turbulent transport in the divertor. This work provides a comprehensive foundation for a first-principles understanding of turbulence in the divertor, which is required for a fully predictive capability for tokamak divertor performance which is, in turn, required for the design of future fusion power plants. The MAST Upgrade device, which is now finished its initial experimental campaign, is ideally positioned to test the results of this article in coming years.

Methods

Experimental database. This paper focusses on results from the Mega Ampere Spherical Tokamak device, MAST⁴¹, during its final experimental campaign in 2013. During these experiments a visible light camera capable of recording in excess of 120,000 frames per second was placed on the divertor with a tangential view into the vessel (see Fig. 1) for several hundred individual plasma discharges. Rather than base this study on individual plasma discharges within this set, a database has been drawn together that covers the widest available parameter range of the plasmas viewed by the camera. Plasma parameters from the database are given in Table 1. The database is constructed of discharges mainly configured in the lower single null (LSN, where only the lower X-point is active) configuration (pictured in Fig. 1) where the data quality is highest, but also considers the impact of resonant magnetic perturbations (used to control violent edge instabilities) and High confinement (H-) mode. The strategy employed in this paper is to compare simulation and experiment, across a wide-ranging experimental database, with robust measurements to draw high-level conclusions around the characteristics of the turbulence, and importantly to validate these aspects of the simulations. With the simulations validated, the flexibility of the code will be leveraged to diagnose the fundamental physics drivers of the turbulence.

Imaging analysis. The method developed and deployed in this article for the tomographic inversion of camera images, described and rigorously tested by ref. 30,42, provides a mapping between the complex image recorded by a high speed camera and a two-dimensional plane in the divertor, taken here as the poloidal (radial-vertical) plane around the inner and outer divertor legs. It assumes that the 3D structures being imaged by the camera align to the background magnetic field (an assumption that is confirmed in simulation). This allows for the formation of a basis on which to perform a tomographic inversion using standard minimisation routines. During the pre-processing stage, subtraction of the pixel-wise minimum of a given frame with its 19 predecessors^{43,44} is applied to isolate fluctuations from the slowly-varying background component of the light. Figure 8 a), b) and d) show an example of a typical camera frame with important features of the plasma indicated. The effect of background subtraction on that frame is shown in panel (b), and the inversion of the background subtracted image onto the inner and outer divertor legs is shown in panel (d). The inversion domain is chosen to isolate the PFR and near SOL region of both divertor legs, avoiding the X-point and core

Table 1 Survey of plasma parameters from MAST and the STORM code used for analysis. The discharge number, confinement mode of the discharge, plasma density $n_{e,sep}$ and electron temperature $T_{e,sep}$ (measured at the upstream separatrix); plasma current I_p ; toroidal magnetic field B_{tor} ; and, input heating power P_{NBI} are shown for all discharges/simulations analysed. RMPs refer to Resonant Magnetic Perturbations for Edge Localised Mode (ELM) control.

Discharge	Confinement mode	$n_{e,sep}$ ($10^{19}m^{-3}$)	$T_{e,sep}$ (eV)	I_p (MA)	B_{tor} (T)	P_{NBI} (MW)
29606	L-mode	0.72	18	0.63	-0.59	0
29608	L-mode	0.97	17	0.63	-0.57	0
29651	L-mode	0.85	24	0.62	-0.55	1.27
29660	L-mode (RMPs)	0.94	25	0.63	-0.54	1.22
29668	L-mode	1.05	27	0.63	-0.56	0.61
29669	L-mode	1.25	19	0.42	-0.51	0.62
29693	L-mode	0.97	32	0.42	-0.48	1.23
29718	L-mode	1.00	38	0.63	-0.54	1.61
29720	L-mode	1.37	29	0.42	-0.47	1.61
29723	H-mode (ELM-free)	1.4	55	0.82	-0.56	1.6
STORM ³⁶	L-mode	0.5	15	0.4	-0.4	0

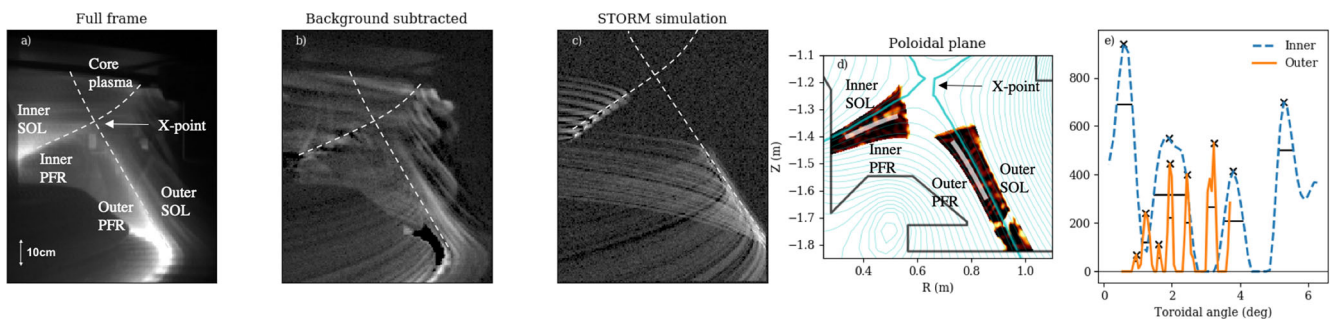


Fig. 8 Example stages of a typical camera data analysis process for divertor turbulence imaging. **a, b** Raw and background subtracted camera data. **c** Synthetic camera data from the STORM simulation (see ref. ³⁶ for simulation details). **d** Tomographically inverted data on sections of the poloidal plane around the inner (closest to the device center) and outer (furthest from device center) divertor legs. White lines indicate line-segments where the emissivity is extracted for analysis in **(e)**, the inverted emissivity from the line segments in **(d)** projected onto the toroidal angle on the $\psi_N = 0.99$ flux surface where ψ_N is the normalised poloidal flux coordinate. Crosses mark detected peak locations, horizontal lines show local Full-Width Half-Maxima.

plasma. The light emission contained in the camera images is dominated by Balmer $3 \Rightarrow 2$ emission and is a complex nonlinear function of plasma quantities—density, temperature and neutral density. Without a multi-measurement comparison, which is extremely challenging for turbulent structures and was not practicable for MAST, the direct experimental inference of these thermodynamic quantities and (more importantly) their fluctuations utilising the diagnostic camera images could not be carried out, though previous studies indicate consistency between camera and probe fluctuation measurements^{26,28}. Instead, this study utilises the turbulence code (STORM) for predictions of the plasma turbulent solution to forward model the Balmer $3 \Rightarrow 2$ light emission observed in synthetic camera image measurements. This provides like-for-like comparison of experiment and simulation, ensuring that any systematic uncertainties are respected in both datasets and allowing high-level comparisons and conclusions to be drawn with confidence.

Computational modelling and synthetic imaging. The STORM model is based on a 3D drift-reduced two-fluid plasma model, with the electron density, n , electron temperature, T , parallel ion velocity U , parallel electron velocity V , and parallel scalar vorticity Ω as dynamic variables. The plasma potential, ϕ , is derived through an inversion of the parallel vorticity, $\Omega = \nabla \cdot (B^{-2} \nabla \phi)$. The set of equations is solved in a field-aligned coordinate system on a grid with toroidal symmetry, with geometric factors derived directly from an equilibrium reconstruction⁴⁵ of the experimental plasma discharge under study, and Bohm sheath boundary conditions are applied at upper and lower divertor boundaries. The grid and geometric properties of the system are not evolved during the simulation. The simulation evolves the full fields (ie no specification of a background profile) and is driven by a particle source centered on the last closed flux surface to mimic neutral ionisation, and an energy source in the core region of the simulation. These sources are scaled until n and T within the simulation match experiment at the outer midplane separatrix, and do not evolve within the simulation. The model makes the cold-ion, Boussinesq, and electrostatic assumptions to make the system tractable in the complex geometry employed for the simulation. The latter is justified by the high resistivity of the SOL and divertor plasma in MAST, however the former two assumptions may impact the detailed characteristics of turbulence in the

simulation. Nevertheless, detailed experimental validation has demonstrated that the STORM model captures the main aspects of SOL turbulence well^{35,36}, and without a more detailed simulation available, is a good basis for a first detailed study of divertor turbulence within this manuscript.

This paper employs synthetic images of the divertor turbulence derived from simulations conducted by ref. ³⁶. Data from the simulation is interpolated onto a grid identical to that used in the experimental analysis, which is then projected along the path of the magnetic field to produce a camera image accounting for line-integration effects and occlusion by machine structures. The emissivity in the poloidal plane is a complex function of thermodynamic quantities of the plasma and neutral gas, and atomic physics, and is forward-modelled in this paper using the OpenADAS database⁴⁶ for the Balmer $3 \rightarrow 2$ transition, employing a neutral particle distribution from a complementary laminar simulation including plasma-neutral interactions. This complementary simulation was conducted with the SOLPS-ITER (Scrape-Off Layer Plasma Simulation - ITER) code⁴⁷, with Monte-Carlo neutral transport and diffusive cross-field plasma transport. The frames are then processed in the same manner as the experimental data. A synthetic camera frame is shown in Fig. 8c). By design the image does not account for any emission from the X-point, core plasma or outer-SOL regions to capture only the salient features of the divertor legs allowing for robust comparison between simulation and experiment.

The use of a fixed, axisymmetric neutral distribution from an auxiliary laminar simulation to generate the D_α emissivity for the synthetic simulation images was the best estimate available, but means that experimental and synthetic images cannot be considered entirely alike. The thermodynamic fluctuations in the plasma may induce fluctuations in the ionisation of neutrals, which cannot be captured in the synthetic images used here since there is no interaction between the turbulence and the neutral gas in the simulation. For this reason the magnitude of the emission is not compared between experiment and simulation, only the geometric positional and geometric properties are compared. It is important to recognise that plasma-neutral interactions are neglected in the turbulent simulation, but are present in the experimental situation, meaning that such an approach to comparison should be limited to leading order turbulent characteristics.

The STORM simulation analysed is in the slightly different lower disconnected double null (LDN) configuration¹, where both X-points are active, but the lower is still

the primary X-point. In the shot studied by Riva et al. the gap between primary and secondary separatrix is between 2 mm and 5 mm. In such a configuration between 5% and 30% of the total power entering the SOL is measured on the lower inner divertor⁴⁸. Reference⁴⁸ also shows that an LSN plasma may have up to twice the power to the lower inner target compared to an LDN, however a wide range of input powers in the LSN configuration has been studied here, with no clear leading order variation in fluctuation properties. As such, this potential variation in power between the LSN and LDN configurations is not considered likely to impact the features of the turbulence studied. Therefore, from the perspective of the PFR of the lower divertor which is the area of study in this paper, the STORM simulation in the LDN configuration is considered sufficiently comparable to an LSN plasma to justify the comparison.

Shape, distribution, and spectra of turbulent structures in the divertor.

Turbulence is complex and difficult to diagnose with acceptable uncertainty. In order to draw robust conclusions, this article focusses on simple and robust measurements that can be readily compared between divertor legs, and between experiment and simulation. The first such set of measurements forms an assessment of the shape and distribution of turbulence structures across the database by calculating a quasi toroidal mode-number (the number of structures in 2π radians toroidally around the device), calculated by counting peaks in the emission along the projection of a magnetic field line in the R-Z plane, and the poloidal structure width calculated as the full-width half maximum of these identified peaks. A useful radial coordinate is the 'poloidal magnetic flux' normalised using values at the magnetic axis ψ_{ax} and separatrix ψ_{sep} , such that $\psi_N = (\psi - \psi_{ax})/(\psi_{ax} - \psi_{sep})$. The analysis is carried out on the flux surface at $\psi_N = 0.99$ which is sufficiently far into the PFR to avoid questions of magnetic field reconstruction misalignment, but sufficiently close to the separatrix that the flux of turbulent structures across the surface is significant. A systematic offset of the experimental flux-surfaces is present which results in a radial shift of measurements by $\Delta\psi_N = 0.005$, though this has little impact on the conclusions of this study.

In Fig. 8 (d) the embedded white lines show the trajectory of the $\psi_N = 0.99$ surface in the R-Z plane in the inner and outer divertor legs, and in (e) the emissivity along the surface is shown in an example discharge. This is cast onto the toroidal angle subtended by the analysed section of the magnetic field line simply by mapping the projection of the magnetic field. By casting this data onto the toroidal angle it is possible to directly compare the features of the inner and outer legs.

Turbulent flow in the inner divertor leg. Since the tomographic inversion employed in this paper produces 2D time-histories in the R-Z plane, flow velocities can be derived by mapping the trajectory of turbulent structures. Velocimetry based on two-point time-delayed cross-correlations has been used here to map the average flow of structures in the inner divertor leg. No clear directive flow was reliably measurable in the outer divertor leg, as demonstrated by the symmetric k_θ spectra in Fig. 4.

Turbulence drives in inner and outer divertor legs. To determine the driving mechanisms for turbulence in the divertor a simulation study has been carried out in the manner of refs. 49,50 by eliminating terms from the vorticity equation, which determines the electrostatic potential and therefore regulates turbulence, that are known to drive certain classes of turbulent transport. The vorticity equation in STORM is [Eq. 1]³⁶

$$\frac{\partial \Omega}{\partial t} + U \mathbf{b} \cdot \nabla \Omega = -\frac{1}{B} \mathbf{b} \times \nabla \phi \cdot \nabla \Omega + \frac{1}{n} \nabla \times \left(\frac{\mathbf{b}}{B} \right) \cdot \nabla P + \frac{1}{n} \nabla \cdot (\mathbf{b} \mathbf{J}_\parallel) + \mu_{\Omega_0} \nabla_\perp^2 \Omega \quad (1)$$

where ϕ is the plasma potential, $\Omega = \nabla \cdot (B^{-2} \nabla_\perp \phi)$ the scalar vorticity, B the magnetic field strength, $P = nT$ the electron pressure, n and T the electron density and temperature, $\mathbf{J}_\parallel = n(U - V)$ the parallel current with U and V the ion and electron velocities parallel to the magnetic field, \mathbf{b} the magnetic field unit vector and μ_{Ω_0} the (small) collisional perpendicular viscosity. This equation has three terms that drive different classes of turbulence. The term $\frac{1}{n} \nabla \times \left(\frac{\mathbf{b}}{B} \right) \cdot \nabla P$ drives interchange turbulence⁵¹, which is analogous to Rayleigh–Taylor turbulence, and is driven by thermodynamic gradients in regions where the curvature of the magnetic field has a destabilising effect. The term $\frac{1}{B} \mathbf{b} \times \nabla \phi \cdot \nabla \Omega$ drives Kelvin–Helmholtz turbulence via sheared flows⁵², whilst the term $\frac{1}{n} \nabla \cdot (\mathbf{b} \mathbf{J}_\parallel)$ term mediates drift-wave turbulence driven ubiquitously by cross-field thermodynamic gradients in a resistive plasma. To test the effect of these three different mechanisms, three simulations were performed beginning from the baseline simulation presented in this paper thus far, with the three turbulent drive terms removed in turn. To remove interchange turbulence from the simulation, $\nabla \times \left(\frac{\mathbf{b}}{B} \right) \rightarrow 0$ was set in the lower divertor. To remove Kelvin–Helmholtz turbulence, $\mathbf{b} \times \nabla \phi \cdot \nabla \Omega \rightarrow \langle \mathbf{b} \times \nabla \phi \cdot \nabla \Omega \rangle_\phi$ in the vorticity equation, whilst to remove drift-waves the substitution $\frac{1}{n} \nabla_\parallel P \rightarrow \langle \frac{1}{n} \nabla_\parallel P \rangle_\phi$ is made in parallel Ohm's law (equation 4 from ref. 36) which blocks energy transfer into resistive drift-waves. $\langle \cdot \rangle_\phi$ indicates a toroidal average in the divertor volume.

Data availability

All data relevant to the analysis and figures within this paper are available from the corresponding author upon request.

Code availability

All codes relevant to the analysis and figures within this paper are available from the corresponding author upon request.

Received: 2 November 2021; Accepted: 6 May 2022;

Published online: 01 June 2022

References

- Buckingham, R. & Loving, T. Remote-handling challenges in fusion research and beyond. *Nat. Phys.* **12**, 391–393 (2016).
- Donne, T. & Morris W. *EUROFusion*: ISBN 978-3-00-061152-0 (2018).
- Kallenbach, A. et al. Impurity seeding for tokamak power exhaust: from present devices via iter to demo. *Plasma Phys Controlled Fusion* **55**, 124041 (2013).
- Loarte, A. et al. Chapter 4: power and particle control. *Nuclear Fusion* **47**, S203 (2007).
- Pitts, R. A. et al. Status and physics basis of the iter divertor. *Phys Scripta* **T138**, 014001 (2009).
- Wenninger, R. et al. Advances in the physics basis of a european demo design. *Nuclear Fusion* **55**, 063003 (2015).
- Nature. <https://doi.org/10.1038/d41586-019-03039-9> (2019).
- Zohm, H. et al. The eu strategy for solving the demo exhaust problem. *Fusion Eng. Design* **166**, 166 (2021).
- Kotschenreuther, M. et al. Magnetic geometry and physics of advanced divertors: The x-divertor and the snowflake. *Phys. Plasmas* **20**, 102507 (2013).
- Valanju, P. M., Kotschenreuther, M., Mahajan, S. M. & Canik, J. Super-x divertors and high power density fusion devices. *Phys. Plasmas* **16**, 056110 (2009).
- Morris, W. et al. MAST Upgrade Divertor Facility: A Test Bed for Novel Divertor Solutions. *IEEE Transact. Plasma Sci.* **46**, 1217–1226 (2018).
- Garcia, O. E., Naulin, V., Nielsen, A. H. & Rasmussen, J. J. Computations of intermittent transport in scrape-off layer plasmas. *Phys. Rev. Lett.* **92**, 165003 (2004).
- D'Ippolito, D. A., Myra, J. R. & Zweben, S. J. Convective transport of intermittent blob-filaments: Comparison of theory and experiment. *Phys. Plasmas* **18**, 060501 (2011).
- Leonard, A. W. Plasma detachment in divertor tokamaks. *Plasma Phys. Controlled Fusion* **60**, 044001 (2018).
- Tsitrone, E. Key plasma wall interaction issues towards steady state operation. *J. Nuclear Mater.* **363**, 12–23 (2007).
- Brooks, J. N. et al. Plasma–surface interaction issues of an all-metal ITER. *Nuclear Fusion* **49**, 035007 (2009).
- Eich, T. et al. Inter-elm power decay length for jet and asdex-upgrade: measurement and comparison with heuristic drift-based model. *Phys. Rev. Lett.* **107**, 215001 (2011).
- Militello, F. et al. Characterisation of the l-mode scrape off layer in mast: decay lengths. *Nuclear Fusion* **56**, 016006 (2016).
- Maurizio, R. et al. Divertor power load studies for attached l-mode single-null plasmas in tcv. *Nuclear Fusion* **58**, 016052 (2017).
- Maqueda, R. J., Stotler, D. P. & the NSTX Team. Intermittent divertor filaments in the national spherical torus experiment and their relation to midplane blobs. *Nuclear Fusion* **50**, 075002 (2010).
- Scotti, F., Zweben, S., Soukhanovskii, V., Baver, D. & Myra, J. Divertor leg filaments in nstx-u. *Nuclear Fusion* **58**, 126028 (2018).
- Terry, J. L. et al. Fast imaging of filaments in the x-point region of alcator c-mod. *Nuclear Mater. Energy* **12**, 989 (2017).
- Ballinger, S. B. et al. Fast camera imaging of plasmas in alcator c-mod and w7-x. *Nuclear Mater. Energy* **17**, 269 (2018).
- Walkden, N. R. et al. Fluctuation characteristics of the tcv snowflake divertor measured with high speed visible imaging. *Plasma Phys. Controlled Fusion* **60**, 115008 (2018).
- Harrison, J. R., Fishpool, G. M. & Dudson, B. D. Filamentary transport in the private flux region in mast. *J. Nuclear Mater.* **463**, 757 (2015).
- Harrison, J. R., Fishpool, G. M., Thornton, A. J., Walkden N. R., & the MAST Team. The appearance and propagation of filaments in the private flux region in mega amp spherical tokamak. *Phys. Plasmas* **22**, 092508 (2015).
- Walkden, N. R. et al. Identification of intermittent transport in the scrape-off layer of mast through high speed imaging. *Nuclear Mater. Energy* **12**, 175 (2017).
- Walkden, N. R. et al. Quiescence near the x-point of mast measured with high speed visible imaging. *Nuclear Fusion* **57**, 126028 (2017).

29. Cavalier, J. et al. Tomographic reconstruction of tokamak edge turbulence from single visible camera data and automatic turbulence structure tracking. *Nuclear Fusion* **59**, 056025 (2019).
30. Farley, T. et al. Filament identification in wide-angle high speed imaging of the mega amp spherical tokamak. *Review of Scientific Instruments* **90**, 093502 (2019).
31. Easy, L. et al. Three dimensional simulations of plasma filaments in the scrape off layer: a comparison with models of reduced dimensionality. *Phys. Plasmas* **21**, 122515 (2014).
32. Walkden, N. R., Easy, L., Militello, F. & Omotani, J. T. Dynamics of 3d isolated thermal filaments. *Plasma Phys. Controlled Fusion* **58**, 115010 (2016).
33. Dudson, B. D., Umansky, M. V., Xu, X. Q., Snyder, P. B. & Wilson, H. R. Bout++: A framework for parallel plasma fluid simulations. *Comput. Phys. Commun.* **180**, 1467–1480 (2009).
34. Dudson, B. D. et al. Recent and current developments. *J. Plasma Phys.* **81**, 365810104 (2015).
35. Militello, F. et al. Multi-code analysis of scrape-off layer filament dynamics in mast. *Plasma Phys. Controlled Fusion* **58**, 105002 (2016).
36. Riva, F. et al. Three-dimensional plasma edge turbulence simulations of the mega ampere spherical tokamak and comparison with experimental measurements. *Plasma Phys. Controlled Fusion* **61**, 095013 (2019).
37. Ryutov, D. & Cohen, B. Geometrical effects in plasma stability and dynamics of coherent structures in the divertor. *Contributions Plasma Phys.* **48**, 48–57 (2008).
38. Simakov, A. N. & Catto, P. J. Drift-ordered fluid equations for field aligned modes in low- β collisional plasma with equilibrium pressure pedestal. *Phys. Plasmas* **10**, 4744 (2003).
39. Katramados, I. et al. Mast upgrade closed pumped divertor design and analysis. *Fusion Eng. Design* **86**, 1595–1598 (2011).
40. Fishpool, G. et al. Mast-upgrade divertor facility and assessing performance of long-legged divertors. *J. Nuclear Mater.* **438**, S356–S359 (2013).
41. Sykes, A. et al. First results from mast. *Nuclear Fusion* **41**, 1423 (2001).
42. Farley T. Analysis of Plasma Filaments with Fast Visible Imaging in the Mega Ampère Spherical Tokamak, *PhD Thesis, Univ. Liverpool* (2020).
43. Dudson, B. D. et al. Experiments and simulation of edge turbulence and filaments in mast. *Plasma Phys. Controlled Fusion* **50**, 124012 (2008).
44. Ayed, N. B. et al. Inter-elm filaments and turbulent transport in the mega-amp spherical tokamak. *Plasma Phys. Controlled Fusion* **51**, 035016 (2009).
45. Lao, L. L. et al. *Nuclear Fusion* **25**, 1611 (1985).
46. Summers H. P. *The ADAS User Manual, version 2.6*, <http://www.adas.ac.uk> (2004).
47. Wiesen, S. et al. The new solps-iter code package. *J. Nuclear Mater.* **463**, 480–484 (2015).
48. Temmermen, G. et al. Thermographic study of heat load asymmetries during mast l-mode discharges. *Plasma Phys. Controlled Fusion* **52**, 095005 (2010).
49. Ricci, P. & Rogers, B. N. Turbulence phase space in simple magnetized toroidal plasmas. *Phys. Rev. Lett.* **104**, 145001 (2010).
50. Rogers, B. N. & Ricci, P. Low-frequency turbulence in a linear magnetized plasma. *Phys. Rev. Lett.* **104**, 225002 (2010).
51. Garcia, O. E., Naulin, V., Nielsen, A. H. & Rasmussen, J. J. Turbulence and intermittent transport at the boundary of magnetized plasmas. *Phys. Plasmas* **12**, 062309 (2005).
52. Lotov, K., Ryutov, D. & Wieland, J. Velocity shear effects in the problem of the electron temperature gradient instability induced by conducting end-walls. *Phys. Scripta* **50**, 153 (1994).

Acknowledgements

This work has been carried out within the framework of the EUROfusion Consortium and has received funding from the Euratom research and training programme 2014–2018 and 2019–2020 under grant agreement No 633053, and through the EPSRC Grant EP/T012250/1. The views and opinions expressed herein do not necessarily reflect those of the European Commission. To obtain further information on the data and models underlying this paper please contact PublicationsManager@ukaea.uk.

Author contributions

N.W.: Lead author, responsible for co-development of the tomographic inversion algorithm utilised in this work, conducting all data analysis presented and drafting this paper. F.R.: Responsible for running simulations utilised within this work and supporting the analysis thereof. J.H.: Responsible for generating experimental data used in this work, and advising and supporting the analysis of experimental camera imaging data. F.M.: Responsible for advising on all aspects of this work. T.F.: Responsible for co-development of the tomographic inversion algorithm utilising in this work. J.O.: Responsible for advising on the simulation analysis aspects of this work. B.L.: Responsible for advising on the overarching objectives and outcomes of this work.

Competing interests

The authors declare no competing interests.

Additional information

Supplementary information The online version contains supplementary material available at <https://doi.org/10.1038/s42005-022-00906-2>.

Correspondence and requests for materials should be addressed to Nicholas Walkden or James Harrison.

Peer review information *Communications Physics* thanks the anonymous reviewers for their contribution to the peer review of this work. Peer reviewer reports are available.

Reprints and permission information is available at <http://www.nature.com/reprints>

Publisher's note Springer Nature remains neutral with regard to jurisdictional claims in published maps and institutional affiliations.



Open Access This article is licensed under a Creative Commons Attribution 4.0 International License, which permits use, sharing, adaptation, distribution and reproduction in any medium or format, as long as you give appropriate credit to the original author(s) and the source, provide a link to the Creative Commons license, and indicate if changes were made. The images or other third party material in this article are included in the article's Creative Commons license, unless indicated otherwise in a credit line to the material. If material is not included in the article's Creative Commons license and your intended use is not permitted by statutory regulation or exceeds the permitted use, you will need to obtain permission directly from the copyright holder. To view a copy of this license, visit <http://creativecommons.org/licenses/by/4.0/>.

© The Author(s) 2022